A GUIDE TO IMPLEMENTATIONAL ASPECTS OF THE SPATIAL-DOMAIN INTEGRAL EQUATION ANALYSIS OF MICROSTRIP ANTENNAS

Louis T. Hildebrand & Derek A. McNamara[1]
Electromagnetism Group, Department of Electrical & Electronic Engineering
University of Pretoria, Pretoria, South Africa 0002

Abstract: In the analysis of microstrip radiating structures integral equation methods rate among the more accurate approaches. By far the most demanding part in the use of these methods is the actual numerical implementation. This paper presents a detailed illustrated description of the numerical implementation of a spatial domain mixed-potential integral equation analysis of microstrip radiating structures.

1. INTRODUCTION

In the analysis of microstrip radiating structures integral equation methods rate among the more accurate approaches. The most widely used is the "full-wave" electric field integral equation (EFIE). When both vector and scalar potentials are used in the formulation of the EFIE, it is often referred to as the mixed-potential integral equation (MPIE). There have been two paths followed in the implementation of the integral equation methods to microstrip geometries; these can be classified according to the manner in which the somewhat cumbersome Green functions appropriate to the problem are dealt with numerically in the moment method solution of the integral equation. In both cases one starts with a Green function derived in analytical form in the spectral domain. Expressions for the moment method matrix elements are then established, consisting of three double integrals, over the spectral domain, domain of the testing functions, and domain of the expansion functions for the unknown current-density, respectively. It is in the evaluation of this expression that two different approaches are used. In the full-wave spatial domain approach this is done by carrying out the integration with respect to the spectral variables numerically in order to convert the Green function to spatial domain form, and then proceeding further with the other two integrations. In the full-wave spectral domain approach, the expression for the moment method matrix elements is manipulated in

such a way that it becomes one consisting of two-dimensional spatial Fourier transforms of the expansion and testing functions (and this can usually be done in closed form) whose product with the original spectral domain Green function must be integrated in the spectral domain. In both cases the moment method solution provides the expansion coefficients of the unknown current-density directly in the spatial domain of course. An exposition of the difference between the two approaches is given by Pozar [1,Sect.IV, Part B].

Published information on the application of the integral equation approaches (no doubt in order to satisfy the space restrictions associated with journal articles) essentially takes the form of some useful suggestions on how to overcome numerical difficulties, but has to stop short of the details needed for a direct implementation of the analysis in a code. This is unfortunate since by far the most demanding part in the use of integral equation analyses for microstrip antenna problems is the actual numerical implementation. One does not always want to ask others directly for their computer codes since these are often not available for distribution for proprietary reasons, or the codes are directly related to the livelihood of the developer who has for this reason invested a considerable amount of time in its development (and this is quite understandable). This paper therefore presents a detailed illustrated description of the numerical implementation of the MPIE analysis of Mosig and Gardiol [2], hereafter simply referred to as *the MPIE formulation*; it is our experience that the discussion on implementation given in [2,3] is the most detailed available in the literature at present. We include the information we would have liked to have had available when we began implementing the techniques of [2,3]. It will be assumed that the reader has references [2], [3] and [4] at hand, although matters will be summarised in Section 2.

---

2. BRIEF OVERVIEW OF THE INTEGRAL EQUATION MODELLING SCHEME

Since the Green functions forming the kernel of the integral equation are those for a horizontal electric current element (at $z=0$) in the presence of a grounded dielectric slab, the only unknowns are the current/charge-densities on the etched conductors. The integral equation is obtained by "replacing" the etched conductors by an equivalent surface current-density $J_s(x,y,0)$ and enforcing the boundary condition that the total tangential electric field at all points on the slab surface occupied by these conductors be set equal to $Z_s(\hat{z} \times J_s)$, where Z_s is the surface impedance of the conducting material. The validity of using the surface impedance concept has been carefully studied by Theron and Cloete [5]. These integral equations are expressed in terms of vector and scalar potentials $\underline{A}(x,y,0)$ and $\Phi(x,y,0)$, respectively, and thus the Green functions used are those associated with these potentials, namely $\underline{G}_A$ and G_V, as described in [2]. A method of moments procedure with sub-sectional expansion and testing functions is used to solve the MPIE, with overlapping rooftop functions in both the x and y directions selected for the expansion functions of the surface current-density. These are placed as follows: the surface of the etched conductor is divided into elementary charge-density cells, with two adjacent charge-density cells forming a current-density cell. Figure 1(a) shows two charge-density cells. The current-density is represented by overlapping rooftop expansion functions. So-called razor test functions, shown in Figure 1(b), which extend along segments linking the centres of adjacent charge-density cells, are used. Although not a fundamental limitation of the technique, we have here arranged matters so that the antenna structure must be segmented into rectangular cells *of equal size*; this simply eases some of the already substantial computational burden.

3. THE DISCRETISED (MATRIX) FORM OF THE INTEGRAL EQUATION

Let there be M of the x-directed rooftop functions, and N of the y-directed ones. Their introduction, along with the razor testing functions extending from the centres of two adjacent charge cells (that is, along C_{xj} in Figure 1), converts the integral equation to the matrix equation $[C][I]=[V]$ which is written [3,4] in terms of sub-matrices as

$$\begin{pmatrix} C^{xx} & C^{xy} \\ C^{yx} & C^{yy} \end{pmatrix} \begin{pmatrix} I_x \\ I_y \end{pmatrix} = \frac{1}{jZ_0} \begin{pmatrix} V_x^{(e)} \\ V_y^{(e)} \end{pmatrix} \qquad (1)$$
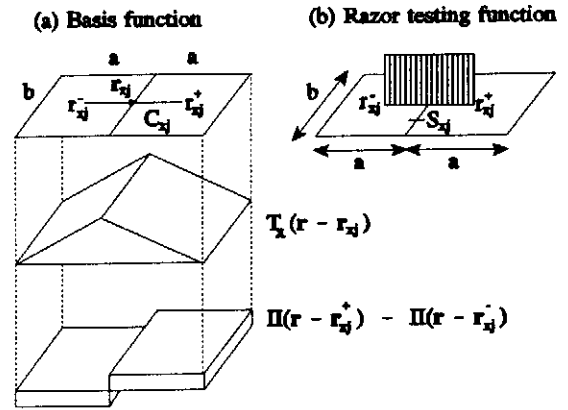

Figure 1 *X-directed current cell with a rooftop basis function and razor testing function. The associated charge distribution over the current cell is also shown.*

Here the C^{xx}, C^{xy}, C^{yx} and C^{yy} are sub-matrices of size MxM, MxN, NxM and NxN, respectively. Thus matrix [C] is of size $(M+N) \times (M+N)$. The elements of the sub-matrices are given by [3,4]

$$C_{ij}^{xx} = \frac{1}{k_0 a k_0 b} \Big[- \Gamma_V(r_{xi}^+|r_{xj}^-) - \Gamma_V(r_{xi}^-|r_{xj}^+) \\ + \Gamma_V(r_{xi}^+|r_{xj}^+) + \Gamma_V(r_{xi}^-|r_{xj}^-) \Big] \\ - \frac{1}{k_0 b} \int_{C_{xi}} \Gamma_A^{xx}(r|r_{xj}) k_0 \, dx + j\frac{Z_s}{Z_0} \frac{a}{b} \delta_{ij} \qquad (2)$$

$$i = 1 \dots M \,, \, j = 1 \dots M$$

$$C_{ij}^{xy} = \frac{1}{k_0 a k_0 b} \Big[- \Gamma_V(r_{xi}^+|r_{yj}^-) - \Gamma_V(r_{xi}^-|r_{yj}^+) \\ + \Gamma_V(r_{xi}^+|r_{yj}^+) + \Gamma_V(r_{xi}^-|r_{yj}^-) \Big] \qquad (3)$$

$$i = 1 \dots M \,, \, j = 1 \dots N$$

In the above, Z_0 is the free space characteristic impedance, k_0 the free space wavenumber and δ_{ij} the Kronecker delta. The Z_s is a surface impedance accounting for the finite conductivity as well as surface roughness and finite thickness of the metallic upper conductor [3]. An expression for C_{ij}^{yy} is obtained by interchanging the couplets (x,y), (a,b) and (M,N) within the expression for C_{ij}^{xx}; reciprocity requires that for cells of equal size $C_{ij}^{yx} = C_{ji}^{xy}$.

I^x and I^y are column sub-vectors of size Mx1 and Nx1, respectively. Their elements are the

coefficients of the x-directed and y-directed expansion functions for the current- density. The excitation column sub-vectors $V_x^{(e)}$ and $V_y^{(e)}$ are similarly of size Mx1 and Nx1, respectively. Thus the column vectors [I] and [$V^{(e)}$] are both of size (M+N)x1.

The precise expression for the elements of [V] depends on the type of excitation geometry being considered. Here a coaxial probe feed will be considered for which a simple, yet sufficiently accurate model was introduced in [3]. This model assumes that the current on the coaxial probe is constant and is therefore only accurate for thin substrates (up to about $\lambda/10$ thick). According to this model the excitation current spreads over a single charge cell as described by the following expression:

$$J_e - \hat{x}\,\frac{I}{4b}\,sgn(x)\left(1 - \frac{2|x|}{a}\right) \qquad (4)$$
$$+\,\hat{y}\,\frac{I}{4a}\,sgn(y)\left(1 - \frac{2|y|}{b}\right)$$

More complex feed models valid for thick substrates are discussed in [6]. The associated excitation surface charge-density distribution over the charge cell is given by a rectangular pulse of value $I/j\omega ab$ where I is the total current carried by the inner coaxial conductor. Figure 2 gives an illustration of the electric surface current-density and charge-density distributions associated with the coaxial probe feed model; note that only the x-directed component is shown in the figure for the sake of clarity. It has been found [7] that the contribution of the excitation *current* (as opposed to the *charge*) to $V^{(e)}$ can usually be neglected; otherwise it must be computed from the expression for Γ_A^{xx} (Γ_A^{yy}) given in (8) with J_{ex} (J_{ey}) replacing T_x (T_y). If we recognise that the matrix elements according to (3) represent the effect of a charge doublet (Figure 1) integrated along a test segment, then since with the above coaxial probe model the excitation is a single pulse of charge (Figure 2), the elements of the excitation vector may be seen to be approximated by [7]

$$V_{xi}^{(e)} - \frac{Z_0}{j\,k_0\,a\,k_0\,b}\,[\,\Gamma_V(r_{xi}^+|r) - \Gamma_V(r_{xi}^-|r)\,]$$
$$\qquad\qquad\qquad\qquad\qquad (5)$$
$$V_{yi}^{(e)} - \frac{Z_0}{j\,k_0\,a\,k_0\,b}\,[\,\Gamma_V(r_{yi}^+|r) - \Gamma_V(r_{yi}^-|r)\,]$$

where feedpoint r is located at the centre of a charge cell. The moment method matrix C is ill-conditioned due to the fact that some rows are almost linear combinations of three other rows. Therefore careful evaluation of its elements is necessary to obtain results of sufficient accuracy. On the other hand, C is diagonally dominant, therefore less stringent accuracy requirements apply to the off-diagonal elements. Certain approximations may then be considered. One of these approximations involves the integral term in (2) which may be approximated as follows:

$$\int_{C_{xi}} \Gamma_A^{xx}(r|r_{xj})k_0\,dx \approx k_0 a \Gamma_A^{xx}(r_{xi}|r_{xj}) \qquad (6)$$

The validity of this approximation is illustrated in Figures 3 and 4 showing the real and imaginary parts, respectively, of both terms in (6). In fact, this approximation may even be considered for the diagonal elements, since the contribution of the vector potential to the value of the matrix element is overshadowed by that of the scalar potential [7]. A conjugate gradient method [8] is used for the iterative solution of the moment method matrix equation.

In (2), (3) and (5) Γ_A^{xx} and Γ_V are *discrete Green functions* (not to be confused with the Green functions themselves) which have as sources complete basis functions as opposed to conventional elementary point sources. $\Gamma_A^{xx}(r|r_j)$ is then the x-component of the vector potential at r created by an x-directed rooftop distribution of surface current at r_j, whereas $\Gamma_V(r|r_{qj})$ is the scalar potential at the same observation point resulting from a rectangular distribution of unit surface charge at r_{qj}. The discrete Green functions are now defined by the following dimensionless expressions [3]:

$$\Gamma_V(r|r_{qj}) - \int_{S_{qj}} \frac{\epsilon_0}{k_0} G_V(r|r')\Pi(r'-r_{qj})k_0^2\,dS' \qquad (7)$$

$$\Gamma_A^{xx}(r|r_{xj}) - \int_{S_{xj}} \frac{1}{\mu_0 k_0} G_A^{xx}(r|r')T_x(r'-r_{xj})k_0^2\,dS' \qquad (8)$$

where μ_0 and ϵ_0 are the permeability and permittivity of free space. A similar expression to that given in (8) holds for Γ_A^{yy}. S_{xj} represents the surface of the current source cell centred at r_{xj} (Figure 1) while the charge source cell centred at r_{qj} extends over S_{qj}. Π is a two-dimensional unit pulse function over S_{qj} and

$T_x(r) = 1 - |x|/a$ over S_{xj}. The Green functions appearing in the above expressions for the discrete Green functions, are given by the following expressions:

$$G_V(r|r') = \frac{1}{2\pi\epsilon_0}\int_0^{\infty} J_0(\lambda R)\frac{\lambda N}{D_{TE}D_{TM}}e^{-u_0 z}d\lambda \quad (9)$$

$$G_A^{xx}(r|r') = G_A^{yy}(r|r') = \frac{\mu_0}{2\pi}\int_0^{\infty} J_0(\lambda R)\frac{\lambda}{D_{TE}}e^{-u_0 z}d\lambda$$

$$(10)$$

where J_0 is the Bessel function of zero'th order and first kind, $D_{TE} = u_0 + u\coth(uh)$, $D_{TM} = \epsilon_r u_0 + u\tanh(uh)$ and $N = u_0 + u\tanh(uh)$; $u_0 = (\lambda^2 - k_0^2)^{1/2}$, $u = (\lambda^2 - \epsilon_r k_0^2)^{1/2}$, h is the substrate thickness and $R = |r - r'|$. For the case of a lossy dielectric, $\epsilon_r = \epsilon_r'(1 - j\tan\delta)$ where $\tan\delta$ is the loss tangent. Figure 5 illustrates the effect of the distance between source and observer (R) on the Green function integrands; the real part of the normalised G_A^{xx} integrand is shown for $R = 0.5\lambda_0$ and $0.05\lambda_0$. It can be seen that when the observer (r) approaches the source point (r'), the zero's of the integrand move away from the origin. In the limiting case $(R = |r - r'| \to 0)$ the first zero tends to infinity, producing a non-oscillating, non-zero function to be integrated over a semi-infinite interval. This produces the singularities in the Green functions at the source point. Now, in the evaluation of the discrete Green functions the situation arises where the observation point r for the potential due to a particular source cell falls within its own source cell boundaries. For this reason the integrands for the discrete Green functions are singular at r due to the Green functions becoming singular. This situation is illustrated in Figures 6 and 7. We will call any evaluation of the potential due to a given source cell at any point in its own source cell a "self term". By now writing (7), in the evaluation of the self term, as

$$\Gamma_V(r_{oj}|r_{oj}) = \epsilon_0 k_0 \int_{S_{0j}} \left[G_V(r_{oj}|r') - G_{Vs}(r_{oj}|r') \right] dS' + \Gamma_{Vs}(r_{oj}|r_{oj}) \quad (11)$$

where an expression for $\Gamma_{Vs}(r_{oj}|r_{oj})$ is given in [3] and

$$G_{Vs}(r_{oj}|r') = \frac{1}{2\pi(\epsilon_r + 1)\epsilon_0|r_{oj} - r'|}$$

$$(12)$$

it is possible to evaluate the scalar potential discrete Green function self term since the difference term in (11) is numerically integrable as illustrated in Figures 8 and 9. Even though the difference term is well-behaved at $r' = r_{oj}$ both terms comprising the difference term, i.e. G_V and G_{Vs}, become singular. The evaluation of the difference term at the source point is therefore done as follows: $G_V(r_{oj}|r_{oj}+\delta) - G_{Vs}(r_{oj}|r_{oj}+\delta)$ where $\delta \to 0$. In this way an accurate estimate of the well-behaved difference term may be obtained at the source point. In similar fashion the singularity in the real part (the imaginary part of the Γ_A^{xx} integrand does not exhibit singular behaviour even in self term evaluations) of the vector potential discrete Green function may be dealt with. In this case, however, an expression for Γ_{As}^{xx} could not be found in the literature, however, analytical integration yields:

$$\Gamma_{As}^{xx}(r_x|0) = \frac{k_0}{2\pi}(a - r_x)\ln\tan\left(\frac{\alpha_1}{2} + \frac{\pi}{4}\right)$$

$$+ \frac{k_0 b}{4\pi}\ln\left[\frac{\tan\left(\frac{\pi}{2} - \frac{\alpha_2}{2}\right)}{\tan\left(\frac{\alpha_1}{2}\right)}\right] + \frac{k_0(a + r_x)}{2\pi}\ln\tan\left(\frac{\alpha_2}{2} + \frac{\pi}{4}\right)$$

$$- \frac{k_0 a}{4\pi}\ln\tan\left(\frac{\alpha_2}{2} + \frac{\pi}{4}\right) + \frac{k_0 b^2}{16\pi a}[\mathrm{cosec}(\alpha_3) - \mathrm{cosec}(\alpha_2)]$$

$$- \frac{k_0 r_x^2}{4\pi a}\ln\tan(\frac{\alpha_2}{2} + \frac{\pi}{4}) + \frac{k_0 b^2}{16\pi a}[\mathrm{cosec}(\alpha_3) - \mathrm{cosec}(\alpha_1)]$$

$$- \frac{k_0(a - r_x)^2}{4\pi a}\ln\tan(\frac{\alpha_1}{2} + \frac{\pi}{4}) + \frac{k_0 r_x b}{4\pi a}\ln\left[\frac{\tan(\frac{\alpha_3}{2})}{\tan(\frac{\alpha_2}{2})}\right]$$

$$-\frac{k_0 r_x}{2\pi a}(a-r_x)\ln\tan(\frac{\alpha_1}{2}+\frac{\pi}{4})$$

$$-\frac{k_0 r_x b}{4\pi a}\ln\left|\frac{cotan(\frac{\alpha_3}{2})}{tan(\frac{\alpha_1}{2})}\right| \qquad (13)$$

where $\alpha_1=\tan^{-1}[b/(2(a-r_x))]$, $\alpha_2=\tan^{-1}[b/(2(a+r_x))]$ and $\alpha_3=\tan^{-1}[b/(2r_x)]$. This expression was derived for an x-directed current cell centred at (0,0) with an observer on the source cell at $\hat{x}r_x$. Therefore, numerical techniques required in the self term evaluation of both the discrete Green functions have now been discussed. For the off-diagonal matrix elements approximations for the discrete Green functions were suggested by Mosig and Gardiol [3]. It is worth mentioning that these approximations have also been implemented successfully by the present authors.
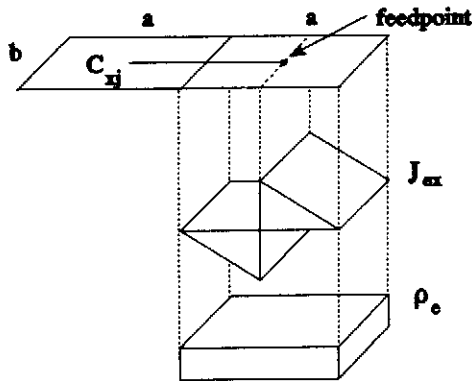
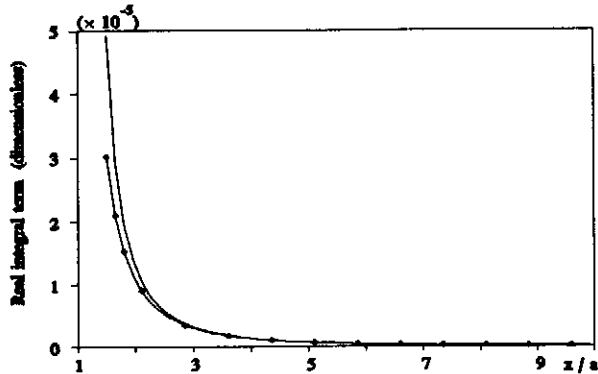**Figure 2** *Electric surface current and charge distributions associated with the coaxial probe feed model.*

Figure 3 *Real parts of the actual integral (————) and approximation (6) (—◇—◇—) suggested by Mosig and Gardiol [1]; f=1.206 GHz, ϵ_r=4.34-j0.0868; h=0.8mm and a=b=6.666 mm.*
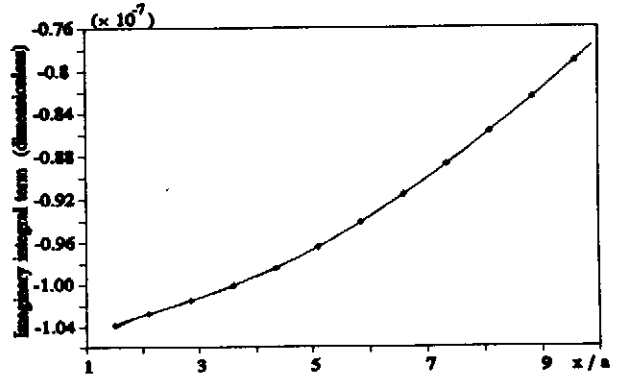
Figure 4 *Imaginary parts of the actual integral (————) and approximation (6) (—◇—◇—) with the corresponding real part shown in Figure 3.*
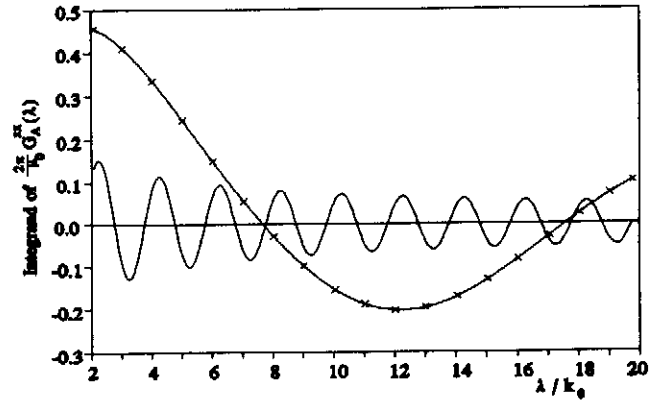
Figure 5 *Normalised integrand of $G_A^{xx}(r/r')$ for R/λ_0=0.5(————) and R/λ_0=0.05(—×—×—) where h/λ_0=0.07 and f=1.206 GHz*
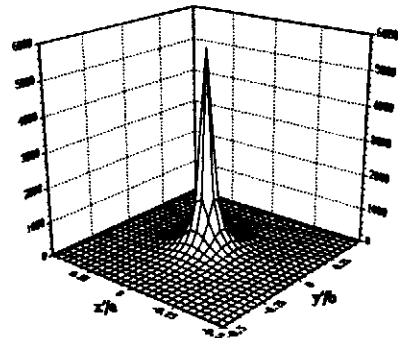
Figure 6 *Real part of the integrand, before pole extraction, in the expression for the Γ_V selfterms.*
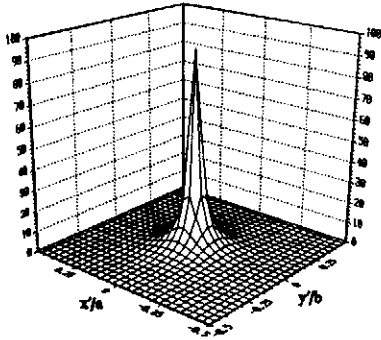
Figure 7 *Imaginary part of the Γ_V integrand corresponding to Figure 6. Note that the maximum value is infinite.*
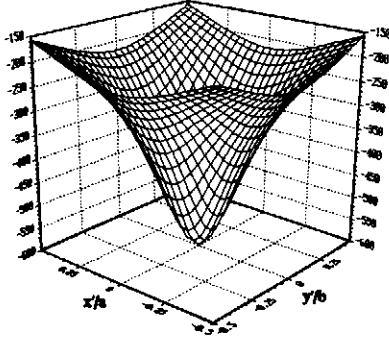

Figure 8 *Real part of the difference term integrand in the evaluation of the Γ_V selfterm.*
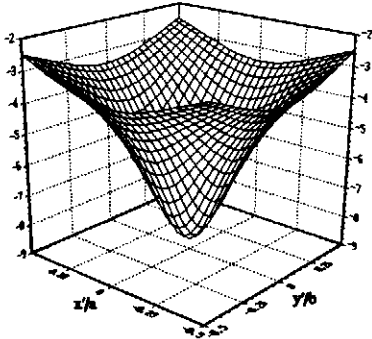

Figure 9 *Imaginary part of the difference term integrand corresponding to the real part shown in Figure 8.*

4. DETAILED ILLUSTRATION AND DISCUSSION OF THE NUMERICAL EVALUATION OF THE ASSOCIATED INTEGRALS

We next consider the evaluation of the Green functions. Figure 10 shows the integrand of $(2\pi/\mu_0)G_A^{xx}$ as a function of λ/k_0 at 1.206 GHz for $\epsilon_r = 4.34 - j0.0868$, and the particular circumstances $h/\lambda_0 = 0.07$ and $R/\lambda_0 = 0.5$ (λ_0 is the free space wavelength). The scalar potential counterpart, i.e. the integrand of $2\pi\epsilon_0 G_V$ as a function of λ/k_0, is shown in

Figure 11. As seen from these figures, discontinuous derivatives, singularities and oscillations in the Green function integrands pose distinct problems, complicating the use of numerical integration techniques. Mosig and Gardiol [9] therefore suggested that the semi-infinite integration intervals in (9) and (10) be subdivided, allowing these problems to be addressed separately. For convenience, the Green function integrals are written as

$$\int_0^\infty F(\lambda)\,d\lambda = \int_0^{k_0} F(\lambda)\,d\lambda +$$

$$\int_{k_0}^{k_0\sqrt{\epsilon_r'}} F(\lambda)\,d\lambda + \int_{k_0\sqrt{\epsilon_r'}}^\infty F(\lambda)\,d\lambda$$

(14)

The numerical difficulties in the evaluation of the Green function integrands in each of these sub-intervals will now be discussed, and the use of proposed solutions illustrated.

4.1 Interval $\lambda \in [0, k_0]$

The term $u_0 = (\lambda^2 - k_0^2)^{1/2}$ appearing in the expressions for D_{TE}, D_{TM} and N introduces branch points in the Green function integrands at $\lambda = k_0$. Manifestations thereof are the discontinuities in the derivatives seen at $\lambda = k_0$ (Figures 10 and 11). Standard numerical integration routines may be inefficient in the integration of functions with such discontinuous derivatives. To obtain accurate numerically integrated estimates for the Green functions over the first interval, Mosig and Gardiol [4] have proposed the substitution $\lambda = k_0 \cos t$. Suppose the integrands may be written as $F(\lambda)$, then this substitution implies that

$$\int_0^{k_0} F(\lambda)d\lambda = \int_{3\pi/2}^{2\pi} F(k_0\cos t)(-k_0\sin t)dt$$

(15)

Figures 12 and 13 show $F(k_0\cos t)(-k_0\sin t)$ as functions of t, with F representing the integrands of $(2\pi/\mu_0)G_A^{xx}$ and $2\pi\epsilon_0 G_V$ shown in Figures 10 and 11 respectively. The integrands are found to be smooth

and easily integrable. In this way then, it is possible to deal with the effect of the branch points in the Green function integrands at $\lambda = k_0$.

4.2 Interval $\lambda \in [k_0, k_0(\epsilon_r')^{1/2}]$

Since the integrand of G_V (9) contains D_{TM} in the denominator, a singularity due to the existence of the dominant TM_0 surface wave mode, appears in the interval $[k_0, k_0(\epsilon_r')^{1/2}]$, as seen from Figure 11. According to a pole extraction technique described in [4], the $2\pi\epsilon_0 G_V$ integrand may be expanded as follows:

$$\frac{J_0(\lambda R)\lambda N}{D_{TE} D_{TM}} = F(\lambda) = [F(\lambda) - F_{sing}(\lambda)] + F_{sing}(\lambda)$$

where $F_{sing}(\lambda) = \text{Res}/[\lambda - (\lambda_p + j\nu_p)]$; Res is the residue of $F(k_\rho)$ (where $k_\rho = \lambda + j\nu$) at pole $k_{\rho\rho} = \lambda_p + j\nu_p$ ($F(\lambda)$ is a special case of $F(k_\rho)$). This leaves $k_{\rho\rho}$ and Res to be determined. The present authors have used Müller's method [10] with deflation to determine $k_{\rho\rho}$ - a root of the univariate complex function $D_{TM}(k_\rho)$. This method is numerically implemented in the IMSL routine ZANLY [11].

The residue may furthermore be determined as follows :

$$\text{Res} = \frac{1}{2\pi j} \oint_C F(k_\rho) dk_\rho = \frac{1}{2\pi j} \int_a^b F(k_\rho(t)) \frac{dk_\rho(t)}{dt} dt \tag{16}$$

where $k_\rho(t) = \lambda(t) + j\nu(t)$, $t \in [a,b]$ and C is *any closed path* around the pole at $k_{\rho\rho}$. A condition, however, is that function $F(k_\rho)$ must be *analytic* inside C except at $k_{\rho\rho}$ [12]. Since C may be represented by *any* closed path around $k_{\rho\rho}$, it is convenient to choose a circle. Then we have $\lambda(t) = r\cos(t)$ and $\nu(t) = r\sin(t)$ as the parametric equations; $t \in [0, 2\pi)$ and r the radius of the circle. The value of r is not important, provided $F(k_\rho)$ is analytic inside the borders of the circle except at $k_{\rho\rho}$. Figure 14 shows the normalised distance $|k_{\rho\rho}/k_0 - 1|$ between the pole at $k_{\rho\rho}$ and the branch point at $\lambda = k_0$ as a function of dielectric thickness (h/λ_0). It can be seen that in the case of electrically thin substrates, the pole due to the surface wave is very close to the branch point. In such cases, radius r must be chosen carefully to avoid the inclusion of the branch point into the borders of the circle inclusion thereof violating the analyticity of $F(k_\rho)$. With the use of (16) and careful selection of r, it is

now possible to numerically determine a value for Res. For instance, at 1.206 GHz ($k_0 = 25.2753$) for $h/\lambda_0 = 0.07$, $R/\lambda_0 = 0.5$, $\epsilon_r = 4.34 - j0.0868$ and $r = 1.0153$ m^{-1} we have Res $= 0.47323 - j0.01815$ where $k_{\rho\rho} = 27.3059 - j0.052039$. Once $k_{\rho\rho}$ and the residue are known, the pole in the G_V integrand may be extracted according to the technique described above; that is

$$\int_{k_0}^{k_0\sqrt{\epsilon_r'}} F(\lambda) d\lambda = \int_{k_0}^{k_0\sqrt{\epsilon_r'}} [F(\lambda) - F_{sing}(\lambda)] d\lambda$$
$$+ \int_{k_0}^{k_0\sqrt{\epsilon_r'}} F_{sing}(\lambda) d\lambda$$

(17)

F_{sing} is analytically integrable [4] while the difference term, which is a well-behaved function, may be integrated numerically. In the lossless case (i.e. for $\tan\delta = 0$) we have $k_{\rho\rho} = \lambda_p$, in other words, the pole due to D_{TM} lies on the λ-axis which is the path of integration. Therefore, at λ_p both terms constituting the difference term in (17), become singular. However, by evaluating $F(\lambda + \delta) - F_{sing}(\lambda + \delta)$ where $\delta \to 0$ it is possible to obtain an accurate estimate of the well-behaved difference term at λ_p. In the case of lossy dielectrics, the pole at $k_{\rho\rho}$ does not lie on the path of integration (Figure 11), nevertheless, strong variations in the integrand due to the pole still require application of this pole extraction technique. An infinite derivative in the difference term integrand at $\lambda = k_0$ may then be eliminated by the substitution $\lambda = k_0\cosh t$. The real and imaginary parts of the G_V difference term integrand, after substitution, are shown in Figure 15; the singularity which has been extracted is visible in Figure 11. If the integrand does not contain D_{TM} in the denominator, the substitution may nevertheless be performed to obtain a smooth integrand at $\lambda = k_0$. This is the case for the Green function $G_A^{xx}(r|r')$, for which Figure 16 gives an illustration of the integrand shown in Figure 10, after substitution. At this point, we are able to accurately determine the integrals in (9) and (10) for $0 \leq \lambda \leq k_0(\epsilon_r')^{1/2}$. This leaves the interval $\lambda > k_0(\epsilon_r')^{1/2}$ which is the subject of the following section.

4.3 The method of averages in the interval $\lambda \in [k_0(\epsilon_r')^{1/2}, \infty]$

As seen from Figures 10 and 11 the Green function integrands show oscillatory behaviour in this interval. Furthermore, these integrands have envelopes which converge very slowly and therefore standard integration routines (such as the trapezium rule and Gauss quadrature) prove to be very inefficient since a large number of integration points is required to achieve reasonable accuracy. Mosig and Gardiol [9] have found a technique known as the *method of averages*, introduced by Hurwitz and Zweifel [13], to be suitable for application to Sommerfeld integrals appearing in microstrip problems. This method is based on the decomposition

$$\int_a^\infty g(\xi R) f(\xi) d\xi - \sum_{n=0}^\infty \int_{a+np/2}^{a+(n+1)p/2} g(\xi R) f(\xi) d\xi$$

(18)

where $g(\xi R)$ is an oscillating function with period p and $f(\xi)$ a smooth, non-oscillating function which behaves asymptotically as $O(\xi^\alpha)$; the integrand therefore diverges for $\alpha > 0$. Although Bessel functions of the first kind - appearing in the Green function expressions - are not strictly periodic, the method of averages may still be applied. However, since the zero's of Bessel functions are not known off-hand the large-argument approximation $J_n(\lambda R) \approx [2/(\pi \lambda R)]^{1/2} \cos(\lambda R - \pi/4 - n\pi/2)$ is used to estimate their zero's. Then we have

$$\xi_m - \left[(m-1) + 0.75 + \frac{n}{2}\right]\frac{\pi}{R}$$

(19)

where ξ_m approximates the m'th zero of $J_n(\lambda R)$. Table 3.1 gives an indication of the accuracy of this approximation in comparing ξ_m (m=1,2,3,4) with the actual zero's of $J_0(\lambda)$ determined numerically with the IMSL routine ZREAL [11]. A question about the validity of this approximation for small R values (source and observation points close to each other) might well arise at this point. In order to answer this question, definite integrals for which the answers are known, were evaluated by the authors using (19) in the method of averages. We know from [14] that

$$\int_0^\infty J_n(\lambda R) d\lambda - \frac{1}{R}$$

(20)

for n > -1. This identity was confirmed for R values ranging from 2.0×10^{-6} to 2.0 and for both n=0 and n=1. Further tests performed by the authors on similar identities lead to the conclusion that (19) will not introduce a significant error, even for small values of R, when used in the method of averages.

m	m'th zero of $J_0(\lambda)$	ξ_m	error (%)
1	2.404825	2.356194	2.02
2	5.520078	5.497787	0.40
3	8.653727	8.639379	0.16
4	11.79153	11.78097	0.08

Table 3.1 Zero's of $J_0(\lambda)$ determined with ZREAL [11] and (19) respectively.

Figure 17 gives the method of averages in the form of a flowchart. The first step is to perform an integration over a half cycle to determine I_m^1.

$$I_m^1 = \begin{cases} \int_a^{\xi_m} g(\xi R) f(\xi) d\xi & (m-1) \\ \\ I_{m-1}^1 + \int_{\xi_{m-1}}^{\xi_m} g(\xi R) f(\xi) d\xi & (m>1) \end{cases}$$

(21)

where ξ_m is the m'th successive zero of the oscillating function g, with $\xi_m > a$. I_{m-1}^2 is then determined through the use of a *weighted mean*

$$I_{m-1}^2 - \frac{w_{m-1}^1 I_{m-1}^1 + w_m^1 I_m^1}{w_{m-1}^1 + w_m^1}$$

(22)

with both I_m^1 and I_{m-1}^1 having been determined previously through integration and with the weights given by $w_m^k = (\xi_1/\xi_m)^{(\alpha+1-k)}$. In general, (22) is given by

$$I_m^k = \frac{w_m^{k-1} I_m^{k-1} + w_{m+1}^{k-1} I_{m+1}^{k-1}}{w_m^{k-1} + w_{m+1}^{k-1}} \qquad (23)$$

If $m-1 \neq 1$ then I_{m-2}^3 is calculated through the use of (23) and the process is repeated until we have I_1^k (where k = m) which will give an approximation of the actual value, I(R), despite the fact that no additional integrations were performed. If the error criterion is not met, I_m^1 (where m = k+1) may be determined through integration, (21), and I_1^{k+1} through repeated application of (23). In this way, an estimate for I(R) may be obtained.

In the determination of the discrete Green function self terms, the situation arises where the distance between source and observer (R) tends to zero. The effect of this, as discussed earlier and illustrated by (19), is that the zero's of the oscillating Green function integrand move further out from the origin along the λ-axis. In the method of averages, weights are determined according to the zero's of the oscillating function, i.e. $w_m^k=(\xi_1/\xi_m)^{(\alpha+1-k)}$. Now it is apparent that, for $\xi_m >> \xi_1$ and k a positive integer which may be large, the weight w_m^k could become a very large real number, creating possible numerical difficulties (numeric overflow or round-off errors, for instance). The present authors have addressed this problem through mathematical manipulation of (23) after which

$$I_m^k = \frac{I_m^{k-1}}{1+\beta}\left[1 + \beta\left(\frac{I_{m+1}^{k-1}}{I_m^{k-1}}\right)\right] \qquad (24)$$

where $\beta = 10\exp\{(\alpha+2-k)[\log_{10}(\xi_1/\xi_{m+1})-\log_{10}(\xi_1/\xi_m)]\}$ is now a manageable real number even though w_m^{k-1} and w_{m+1}^{k-1} are very large. Consider for example a situation where $\xi_1=200$, $\xi_{50}=8\times10^3$, $\xi_{51}=8.1\times10^3$, k=50 and $\alpha=0$; then we have $w_{50}^{49}=7.923\times10^{76}$ and $w_{51}^{49}=1.438\times10^{77}$ whilst $\beta = 1.815$!. Therefore, to avoid numerical difficulties which may be encountered in a straightforward application of (23), we propose (24) as a means to determine I_m^k.
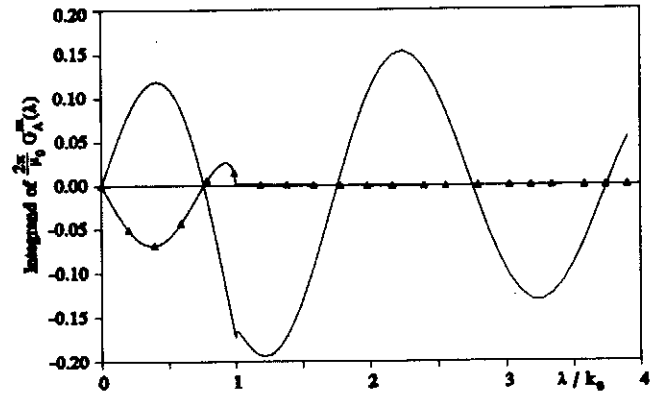

Figure 10 Real (———) and imaginary (—△—△—) integrands of $(2\pi/\mu_0)G_A^{xx}$ for $\epsilon_r=4.34-j0.0868$, $h/\lambda_0=0.07$ and $R/\lambda_0=0.5$.
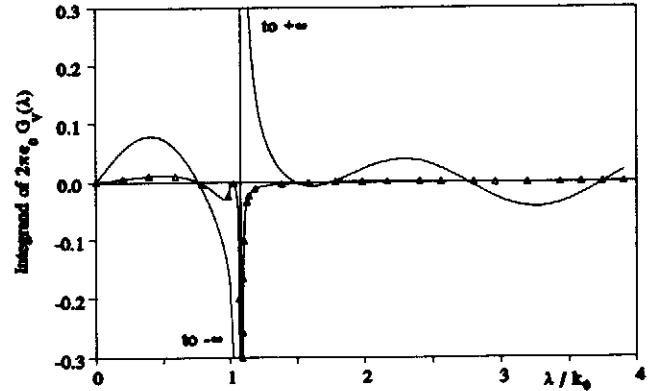

Figure 11 Real (———) and imaginary (—△—△—) integrands of $2\pi\epsilon_0 G_V$ for $\epsilon_r=4.34-j0.0868$, $h/\lambda_0=0.07$ and $R/\lambda_0=0.5$ at 1.206 GHz.
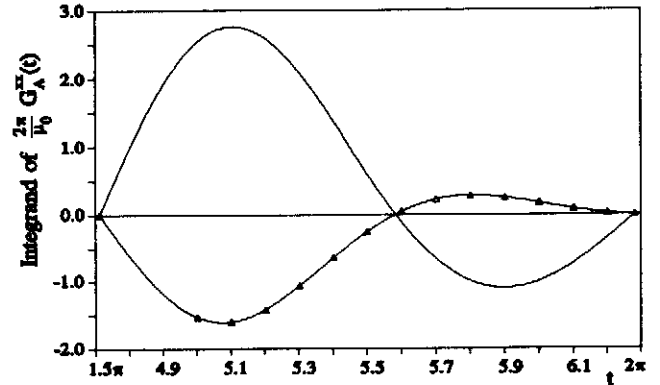

Figure 12 Real (———) and imaginary (—△—△—) integrands of $(2\pi/\mu_0)G_A^{xx}$ for $\lambda \in [0,k_0]$ after substitution $\lambda=k_0\cos t$.
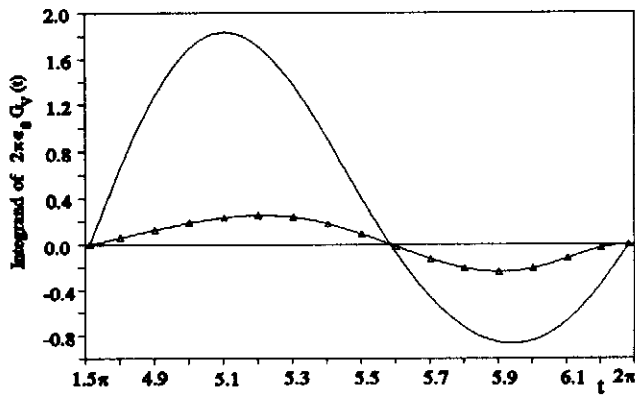
Figure 13 *Real (————) and imaginary (—△—△—) integrands of $2\pi\epsilon_0 G_V$ in the interval $\lambda \in [0,k_0]$ after substitution $\lambda = k_0 \cos t$.*
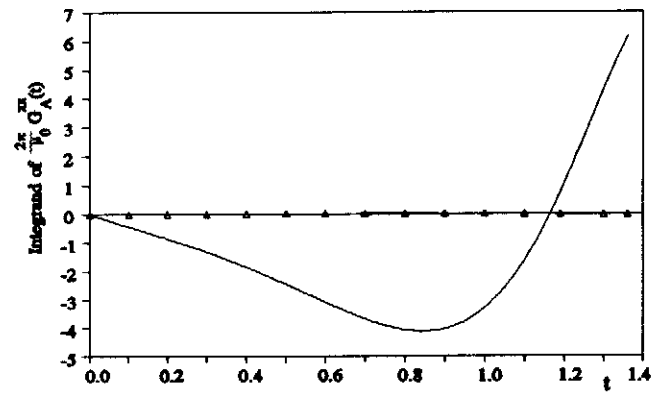

Figure 16 *Integrand of $(2\pi/\mu_0)G_A^{xx}$ (real (————) and imaginary (—△—△—△—)) after substitution.*
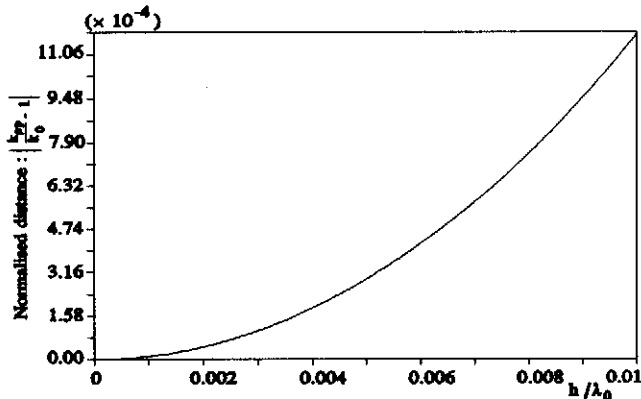

Figure 14 *Normalised distance between the pole due to D_{TM} and the branch point due to u_0 as a function of dielectric thickness, i.e. $|k_{ap}/k_0-1| (h/\lambda_0).$*

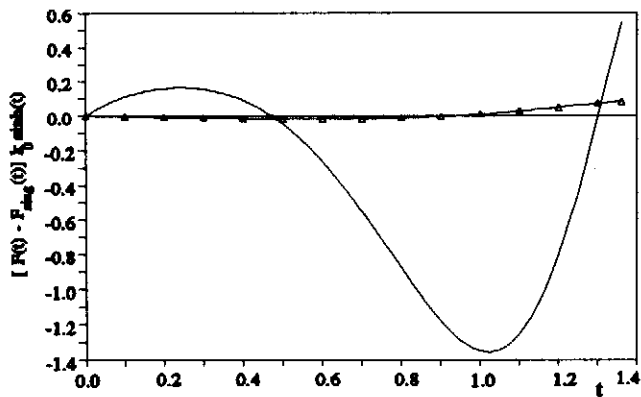**Figure 15** *$2\pi\epsilon_0 G_V$ difference term integrand (real (————) and imaginary (—△—△—△—)) after substitution $\lambda = k_0 \cosh t.$*

Figure 17 *Flowchart for the method of averages*

5. INTERPOLATION

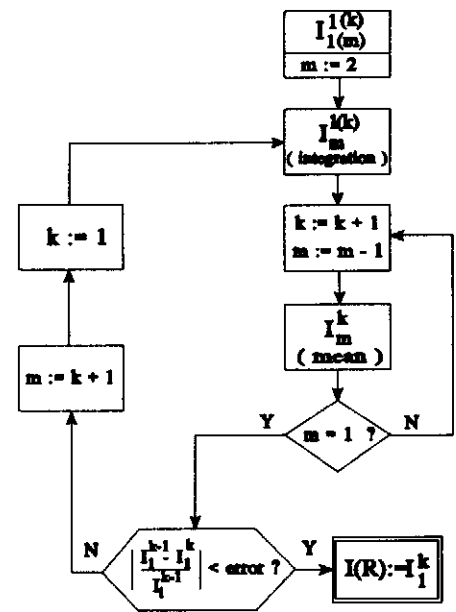As discussed in the previous section, the evaluation of the Green functions require implementation of numerical integration routines. This is in addition to the numerical integration which has to be performed in the evaluation of the discrete Green functions (which contain the Green functions). With these discrete Green functions it is now possible to compute the moment method matrix elements whose solution yields the unknown coefficients I_x and I_y. However, in order to reduce the computation time, Mosig and Gardiol, noting the fact that the relevant Green functions are only dependent on the distance between source and observer (and not the relative orientation), consequently suggest the use of an interpolation table to evaluate the Green functions. This interpolation table consists of a discrete set of Green function

values tabulated against a set of distances R_i where $i=1..P$ and $R_{min} < R_i < R_{max}$. Interpolation is then used to evaluate these functions at any distance ranging from R_{min} to R_{max} (the maximum linear dimension of the structure). It is suggested that convergence tests be performed to determine optimum values for P (typically from 50 to 250) related to specific problems. Since the value of R_{min} has an effect on the self term evaluation of the discrete Green functions, care should be taken when choosing values for R_{min}. However, numerical experiments performed by the present authors, showed differences on the order of 0.1% in the self term values computed for $R_{min}=10^{-4}$ and for $R_{min}=10^{-11}$. Furthermore, careful consideration should be given to the computation of R_i. In this regard, the following expressions have been used to good effect:

$$R_i - R_{min}\left(\frac{R_{inter}}{R_{min}}\right)^{\left(\frac{i-1}{N-1}\right)} \quad (25a)$$

for $R_{min} < R < R_{inter}$ and

$$R_i - R_{inter} + \left(R_{max} - R_{inter}\right)\left(\frac{i-1}{N-1}\right) \quad (25b)$$

for $R_{inter} < R < R_{max}$ where $R_{inter} = (a^2+b^2)^{1/2}$. With interpolation it is possible to reduce the computation time without sacrificing significant accuracy.

6. COMPUTATION OF FAR-ZONE RADIATION

In solving for the surface current distribution, we are interested in the case where both source and observer are located on the air-dielectric interface i.e. where $z=0$. For far-field radiation computation, on the other hand, this will not be the case. If the radiator is placed in the xy-plane, far-field radiation on broadside now implies that z becomes large and then the following situation arises: since u_0 is purely imaginary in the interval $0 \leq \lambda < k_0$, and z a very large real number, $\exp(-j(k_0^2-\lambda^2)^{1/2}z)$ causes rapid sign changes in this interval. Furthermore, since u_0 is real for $\lambda \geq k_0$ we have $\exp(-u_0 z) \rightarrow 0$ and thus the integration interval in effect reduces to $0 \leq \lambda < k_0$. An example of a Green function integrand for $z=5.0$ m

is shown in Figure 18 which illustrates the rapid sign changes and reduced integration interval just spoken of. From this figure it is clear that standard numerical integration routines would not be capable of yielding accurate estimates of the Green function integrals with large z values. We therefore resort to *asymptotic techniques* to obtain approximate analytic solutions. Application of the *method of steepest descent* [15] to these integrals yields the following far-field radiation expressions for arbitrarily shaped etched antennas in terms of the coefficients I_x and I_y [3]:

$$E_\theta - G_E^{\theta x}(r|0)\sum_{i=1}^{M} aI_{xi}e^{jk_0 g_i} + G_E^{\theta y}(r|0)\sum_{j=1}^{N} bI_{yj}e^{jk_0 g_j} \quad (26)$$

$$E_\phi - G_E^{\phi x}(r|0)\sum_{i=1}^{M} aI_{xi}e^{jk_0 g_i} + G_E^{\phi y}(r|0)\sum_{j=1}^{N} bI_{yj}e^{jk_0 g_j} \quad (27)$$

where $g_k = x_k \sin\theta\cos\phi + y_k \sin\theta\sin\phi$ $(k=i,j)$; x_k and y_k are the centre coordinates of the k'th current cell. We also have

$$G_E^{\theta x}(r|0) - \frac{-jZ_0\cos\phi f_\theta(\theta)}{\lambda_0}\frac{e^{-jk_0 r}}{r} \quad (28)$$

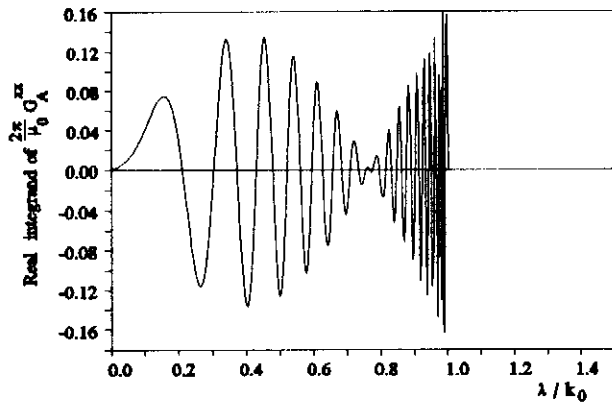$$G_E^{\phi x}(r|0) - \frac{jZ_0\sin\phi f_\phi(\theta)}{\lambda_0}\frac{e^{-jk_0 r}}{r} \quad (29)$$

$$G_E^{\theta y}(r|0) - \frac{-jZ_0\sin\phi f_\theta(\theta)}{\lambda_0}\frac{e^{-jk_0 r}}{r} \quad (30)$$

$$G_E^{\phi y}(r|0) - \frac{-jZ_0\cos\phi f_\phi(\theta)}{\lambda_0}\frac{e^{-jk_0 r}}{r} \quad (31)$$

$$f_\theta(\theta) - \frac{T\cos\theta}{[T - je_r\cos\theta\,cotan(k_0 hT)]} \quad (32)$$

$$f_\phi(\theta) - \frac{\cos\theta}{[\cos\theta - jT cotan(k_0 hT)]} \quad (33)$$

$$T - \sqrt{(\epsilon_r - \sin^2\theta)} \qquad (34)$$

Figure 18

Figure 18 *Normalised real integrands of G_A^{xx} (i.e.*
$J_0(\lambda R)\lambda exp(-u_{0}z)/D_{TE}$ for $R/\lambda_0=0.5$ and $h/\lambda_0=0.07$ at $f=1.206$ GHz
and $\epsilon_r=4.34-j0.0868$) for $z = 0.0$ and 5.0 m.

7. SUMMARY

The MPIE formulation rates among the accurate integral equation analysis techniques for microstrip radiating structures. After a brief overview of the modelling scheme, numerical techniques used by the authors in the implementation of the formulation were discussed: a detailed and illustrated discussion of the numerical evaluation of the required Green functions was given, an interpolation method used to improve the computational efficiency was discussed and finally the computation of far-field radiation patterns was considered. A FORTRAN computer code implementation of the MPIE formulation is available on request from the second author.

References

[1]   D.M.Pozar, "Microstrip antennas", *Proc.IEEE*, Vol.80, No.1, pp.79-91, Jan.1992.

[2]   J.R.Mosig & F.E.Gardiol, "A dynamical radiation model for microstrip structures" in P.Hawkes (Edit.) : *Advances in Electronics and Electron Physics (Academic Press,1982)* pp.139-327.

[3]   J.R. Mosig and F.E. Gardiol, "General integral equation formulation for microstrip antennas and scatterers," *IEE Proc.*, vol. 132, Pt.H, no. 7, Dec. 1985.

[4]   J.R. Mosig and F.E. Gardiol, "Numerical analysis of microstrip patch antennas" in J.R.James & P.S.Hall (Edits.) : *Handbook of Microstrip Antennas* (Peter Peregrinus Ltd.,1989).

[5]   I.P. Theron & J.H. Cloete, "On the use of the Leontovich boundary conditions in the analysis of microstrip antennas", *1992 IEEE AP-S Symposium*, pp. 620-623.

[6]   R.C. Hall, J.R. Mosig and F.E. Gardiol, "Analysis of microstrip antenna arrays with thick subtrates", *Proc. 17 th European Microwave Conf.*, Rome, 1987.

[7]   J.R. Mosig, Laboratoire d'Electromagnetisme et d'Acoustique, Ecole Polytechnique Federale de Lausanne, Lausanne, Switzerland. Private communication.

[8]   M. Hestenes and E. Stiefel, "Method of conjugate gradients for solving linear systems," *J. Res. Natl. Bur. Stand.*, vol. 49, pp. 409-436, 1952.

[9]   J.R. Mosig and F.E. Gardiol, "Analytic and numerical techniques in the Green's function treatment of microstrip antennas and scatterers," *IEE Proc.*, vol. 130, Pt.H, no. 2, pp. 175-182, March 1983.

[10]   D.E. Müller, "A method for solving algebraic equations using an automatic computer", *Math. Tables Aids Comput.*, vol. 10, pp. 208-215, 1956.

[11]   IMSL Inc., Houston, Texas, USA. Library of Fortran Routines for Mathematical Application, Version 1.0, April 1989.

[12]   E. Kreyszig, *Advanced Engineering Mathematics* (John Wiley & Sons, 1988).

[13]   H. Hurwitz and P.F. Zweifel, "Numerical quadrature of Fourier transform integrals," *Math. Tables Aids Comput.*, vol. 10, pp. 140-149, 1956.

[14]   M.R. Spiegel, *Mathematical handbook* (McGraw-Hill, 1968).

[15]   L.B. Felsen and N. Marcuvitz, *Radiation Scattering of Waves* (Prentice_Hall, 1973).